Analysis of the Signal Combiner for Multiple Antenna Arraying

R. A. Winkelstein
Communications Systems Research Section

The signal-to-noise ratio of video data received from the second Mariner 73-Mercury encounter was improved by arraying two available 26-m antennas with the 64-m antenna normally used for reception. Specially designed digital equipment was used to combine the signals received by the three antennas. Analysis of this equipment shows that the received signals which arrived with relative time differences up to 50 μs were correctly aligned by the combining equipment to an accuracy within 50 ns. Observed error rates during the encounter track verified the system improvement to within 0.1 dB of the predicted 0.8 dB value.

I. Introduction

On September 21, 1974, the two 26-m antennas at DSSs 12 and 13 were arrayed with the 64-m antenna at DSS 14 to enhance the received video data from the second Mariner 73 Mercury encounter. The signals received at each of the three antennas were first translated to baseband frequency by coherent mixing with the carrier frequency. Then the baseband signals from the two smaller antennas were sent to DSS 14 over the microwave link. The baseband signal received at the DSS 14 antenna was given a fixed delay by sending it over a round-trip route on the microwave link. After arrival over the microwave link at DSS 14, the three baseband signals were fed to specially designed digital equipment whose function was to align the signals time-wise to each other and combine them for further processing by the DSS 14 receiver.

A description of the signal combining equipment has been given by H. Wilck (Ref. 1). This report describes the analysis techniques used to design the combining equipment and to predict its performance during the Sept. 21 encounter.

II. Signal Combination

Table 1 lists the relevant signal parameters predicted for the encounter on September 21. These parameters provided the main design criteria for the combining equipment and were within the measurement tolerances

of the actual values. Requirements on the signal combining equipment were twofold. First, the three baseband signals had to be automatically and continuously aligned timewise so that the data components of the signals would add coherently when the signals were summed. Secondly, the signals had to be summed using optimal summing ratios to provide the maximum possible signal-to-noise ratio in the combined output signal.

A block diagram of the signal combiner is shown in Fig. 1. The three baseband signals first pass through variable attenuators which are adjusted to provide equal readings on the power meters. The signals from DSSs 12 and 13 are then filtered to prevent aliasing by analog-to-digital conversion equipment in the phase tracking channels. These phase tracking channels align the signals to match the signal from DSS 14, which is used as the reference. The three signals are then summed to provide the optimum signal-to-noise ratio at the output of the summing amplifier. A filter in front of the power meter monitoring the signal from DSS 14 is used to provide an equal noise bandwidth for comparison to the other two power meter readings.

The baseband signals may be considered to consist of a signal power, S_i, plus a noise power, N_i, $i = 1,2,3$, where the value of i corresponds to each of the three antennas. Therefore, the signal-to-noise ratio of the baseband signal from the ith antenna is

$$SNR_i = \frac{S_i}{N_i} \tag{1}$$

Assuming that the noises in the three baseband signals are uncorrelated to each other so that noise power adds linearly as contrasted to the fact that signal data voltages add linearly, the signal-to-noise ratio, SNR_s, at the output of the summing amplifier is

$$SNR_s = \frac{(\sqrt{S_1} + \alpha_2\sqrt{S_2} + \alpha_3\sqrt{S_3})^2}{N_1 + \alpha_2^2 N_2 + \alpha_3^2 N_3} \tag{2}$$

where α_i is a voltage attenuator ratio at the ith input to the summing amplifier, α_1 is set to unity. Eq. (2) is maximized when

$$\alpha_2 = \frac{N_1\sqrt{S_2}}{N_2\sqrt{S_1}}, \qquad \alpha_3 = \frac{N_1\sqrt{S_3}}{N_3\sqrt{S_1}} \tag{3}$$

Under these conditions, Eq. (2) becomes

$$SNR_s = SNR_1 + SNR_2 + SNR_3 = SNR_1 \cdot A_r \tag{4}$$

where

$$A_r = 1 + \frac{SNR_2}{SNR_1} + \frac{SNR_3}{SNR_1} \tag{5}$$

The ratio of SNRs in Eq. (5) are equal to the ratio of R's in Table 1, from which

$$\frac{SNR_2}{SNR_1} = \frac{SNR_3}{SNR_1} = -10\,\text{dB} = 0.1 \tag{6}$$

Eq. (5) therefore becomes

$$A_r = 1.2 = 0.8\,\text{dB} \tag{7}$$

Thus, adding the received signals from the two smaller antennas to the signal received by the larger antenna provides an improved signal-to-noise ratio of 0.8 dB compared to the use of the larger antenna alone.

To determine the sensitivity of A_r in Eq. (5) to nonoptimum values of α_i, Eq. (3) is modified to

$$\alpha_2 = \theta_2 \frac{N_1\sqrt{S_2}}{N_2\sqrt{S_1}}, \qquad \alpha_3 = \theta_3 \frac{N_1\sqrt{S_3}}{N_3\sqrt{S_1}} \tag{8}$$

where α_2 and α_3 vary from optimum as θ_2 and θ_3 vary from unity. Eq. (4) then becomes

$$SNR_s = SNR_1 \cdot B_r \tag{9}$$

where

$$B_r = \frac{\left(1 + \theta_2 \frac{SNR_2}{SNR_1} + \theta_3 \frac{SNR_3}{SNR_1}\right)^2}{1 + \theta_2^2 \frac{SNR_2}{SNR_1} + \theta_3^2 \frac{SNR_3}{SNR_1}} \tag{10}$$

The loss in improvement due to nonoptimum α_i is the ratio of B_r to A_r and is plotted in dB in Fig. 2 for variations in θ, and hence in α, up to $\pm 30\%$. From Fig. 2, it is seen that the loss is less than 0.07 dB when α_2 and α_1 are within 30% of optimum.

The actual values of α_2 and α_3 indicated in Fig. 1 may be determined by noting that the power inputs, P_i, to the summing amplifier are

$$P_i = S_i + N_i \tag{11}$$

From Table 1

$$R_i = \frac{S_i T_B}{N_{oi}} \tag{12}$$

where T_B is the data bit time, the reciprocal of the data rate, and N_{oi} is the one-sided noise spectral density for the ith input to the summing amplifier. Moreover,

$$N_i = N_{oi}B \tag{13}$$

where B is the low-pass filter one-sided noise bandwidth. For a 1-MHz resistance-capacitance (RC) low-pass filter, B is 1.57 MHz. Using Eqs. (11), (12), and (13), Eq. (3) becomes

$$\alpha_2 = \sqrt{\frac{P_1R_2(R_2 + T_BB)}{P_2R_1(R_1 + T_BB)}}, \qquad \alpha_3 = \sqrt{\frac{P_1R_3(R_3 + T_BB)}{P_3R_1(R_1 + T_BB)}} \tag{14}$$

For equal powers, Eq. (14) gives α_2 and α_3 equal to 0.3.

III. Phase Tracking Channel

The heart of the signal combiner is the phase tracking channel. Its function is to provide a continuously variable amount of time delay in order to match the signal at the summing amplifier to the reference baseband signal from DSS 14. This variable delay compensates for the change in signal arrival time at the different antennas as the Earth rotates during the mission viewing period. The time delay variations listed in Table 1 include the fixed microwave link delay time from the 26-m antennas to DSS 14, because the signal combining equipment is located at DSS 14. Since the phase tracking channel can provide only positive time delays, the baseband signal is given a fixed delay of 110 μs by sending it through the microwave link on a round-trip route.

A block diagram of phase tracking channel A is shown in Fig. 3. Equipment shown for channel A below the broken line in Fig. 3 is duplicated for channel B. The baseband signal from DSS 13 is converted to digital form by an 8-bit analog-to-digital (A/D) converter sampled at approximately a 2.5-MHz rate. These digital values are placed in a first-in first-out (FIFO) memory system which provides the proper amount of time delay. The digital values are read out of the FIFO at a fixed 2.5-MHz rate, reconverted to analog form by an 8-bit digital-to-analog (D/A) converter, and then added to the other baseband signals in the summing amplifier.

Sign bits from the FIFO output are compared to sign bits of the DSS 14 baseband signal obtained from a 1-bit A-D converter. This comparison is carried out and averaged by the quadrature correlator for periods of one second. At the end of each second, the quadrature correlator develops a digital number directly proportional to the phase timing error between the two signals. This digital number or count is scaled by a digital attenuator and converted to an analog control voltage by the 16-bit (D/A) converter. The scaling factor of the digital attenuator is preset by a manual front panel control for an optimum tradeoff between the loop transient and noise responses.

The control voltage out of the 16-bit D/A converter is used to control the search oscillator of a frequency synthesizer. This causes a slight change, Δf, in the 2.5-MHz synthesizer output frequency used to strobe the FIFO input. As a result, the FIFO system delay is changed in the direction to force the error count out of the quadrature correlator to zero. At this time, the two signals are in phase, and the output count developed by the in-phase correlator is at a maximum. The in-phase correlator count is displayed on the front panel and is used to aid the initial loop acquisition and to indicate correct system operation.

Analysis of the phase tracking channel control loop may be carried out by aid of the Laplace block diagram of Fig. 4. Here the input to the loop is taken to be the time offset between the channel input baseband signal and the DSS 14 baseband reference signal. The output is the loop error signal and is equivalent to the timing error between the two baseband signals as seen by the summing amplifier. A key requirement of the loop analysis is to determine the limits of the various components of this output error.

A. Control Loop Description

1. FIFO memory system. The FIFO memory system consists principally of the FIFO memory and the fill counter as is shown in Fig. 5. The memory can hold up to 512 8-bit words which are input to the memory using the input strobe, and output from the memory using the output strobe. These strobes are independent of each other and are generated asynchronously. However, as the name "first-in first-out" suggests, the sequence of words out from the memory is the same as the sequence of words into the memory.

The resident time of a particular 8-bit word in memory is the delay time, and is proportional to the number of words in the memory as indicated by the fill counter. If the input strobe is slightly higher in frequency than the

output strobe, the memory will gradually fill until the FIFO FULL signal becomes true. Conversely, if the input strobe is slightly lower in frequency than the output strobe, the memory will gradually empty until the FIFO EMPTY signal becomes true. The fill counter obtains the count number by counting the difference between the input strobes and output strobes. This count number is also displayed on the front panel to aid in acquisition and to indicate correct equipment operation by comparison to precalculated values. The reset signal sets both the memory and counter to zero when the system is reset or initially started.

In terms of the Laplace block diagram (Fig. 4) the FIFO memory system produces an output time difference between the two baseband signals as a function of the input frequency Δf indicated in Fig. 3. The FIFO memory operation is similar to that of an integrator in that the rate of change of time delay is proportional to Δf. Accordingly, the Laplace transfer function of the system is given as G_f/s, where s is the Laplace complex frequency and G_f is the system gain constant. At a 2.5-MHz strobe rate, each word in memory represents a 0.4 μs time delay. Thus G_f is 0.4 μs/Hz/s.

2. In-phase correlator. Although the in-phase correlator is not part of the phase tracking control loop, its description is prerequisite to a description of the quadrature correlator. The correlation of two signals is simply the average of their product. When the signals to be correlated are represented by only their respective sign bits, as is done in the phase tracking control loop, then this product is most easily generated by an exclusive-or circuit, as is shown in Fig. 6. V_1 and V_2 are the baseband signal voltages. The exclusive-or circuit activates a counter which is incremented when V_1 and V_2 are the same and decremented when V_1 and V_2 are different.

At the end of each second, the accumulated count in the in-phase correlator is stored in a front panel display for operational verification. The counter is then reset to zero in preparation for the next second's count. Since the signals are input at the digitized rate of 2.5 MHz, the count for noise-free in-phase signals can reach a maximum of 2.5 million. Thus 7 binary coded decimal (BCD) digits are required in the counter.

Normalized plots of the output count as a function of the delay, τ, of V_2 with respect to V_1 are shown in Fig. 7. Normalization of these plots, known as correlation curves, assigns a value of unity as the maximum count generated. Fig. 7(a) is the correlation curve of signals which contain only the square wave subcarrier frequency. τ_1 is the quarter period of the subcarrier frequency. From Table 1, τ_1 is found to be 1.41 μs. $C_1(\tau)$ and $C_2(\tau)$ are equations of the indicated portions of the correlation curve.

Fig. 7(b) is the correlation curve of signals containing no subcarrier frequency, but rather only random data known as pseudo-noise (PN) data. τ_2 is the data period, which from Table 1 is found to be 8.5 μs. The correlation curve of actual signals containing both subcarrier frequency and PN data is shown in Fig. 7(c). This curve is the product of the curves in Figs. 7(a) and 7(b). The bracketed expression in Fig. 7(c) indicates the correlation of the time function signals V_1 and V_2.

3. Quadrature correlator. The quadrature correlator, similar to the in-phase correlator, each second produces a count which is a function of the relative signal delay. To be useful as a control element in a tracking loop, the quadrature correlator should produce a count of zero when the input signals are exactly aligned. When the signals are not aligned, the count should be proportional to the time difference, τ. Such a correlation curve is obtained by advancing and delaying the correlation curve of Fig. 7(c) by an amount γ as shown respectively in Figs. 7(d) and 7(e). The desired correlation curve is half the difference of the curves in Figs. 7(d) and 7(e) as shown in Fig. 7(f). The equation of the control portion of the curve in Fig. 7(f) is obtained in a step by step manner from the previous curves of Fig. 7 and is found to be

$$C_7(\tau) = -\left(\frac{1}{\tau_1} + \frac{1}{\tau_2} - \frac{2\gamma}{\tau_1\tau_2}\right)\tau \qquad (15)$$

Fig. 8 shows the quadrature correlator which provides the correlation curve of Fig. 7(f). The delay γ is obtained from the four-bit shift registers. Since the shift registers are clocked at the data rate of 2.5 MHz, each bit provides a delay of 0.4 μs. Therefore γ is 1.6 μs and $C_7(\tau)$ is found to be $-0.56\ \tau$.

The quadrature correlator count represents an integral of the input signal phase difference averaged over a time period of one second. After each second, the quadrature correlator count register is reset to zero as is the in-phase correlator counter. Hence the operation of the quadrature correlator is equivalent to that of an integrate-and-dump circuit with gain constant G_c shown in Fig. 4. G_c, the

product of the magnitude of the slope of Eq. (15) and the normalization factor K, is

$$G_c = 0.56\,K \text{ counts}/\mu\text{s}/\text{s} \tag{16}$$

where K, the normalization constant for the curves in Fig. 7, is the counts per second displayed by the in-phase correlator when the signals are aligned.

It may be noted that G_c of Eq. (16) is somewhat dependent on the type of data being transmitted. Thus Eq. (16) is strictly true only for PN data. For the extreme case of all zeros data or all ones data, G_c becomes 0.71 K. At the opposite extreme of alternating ones and zeros data, G_c is found to be 0.41 K. Therefore the G_c of Eq. (16) is within 27% of any data type actually transmitted.

The Laplace block of an integrate-and-dump circuit, shown as the quadrature correlator in Fig. 4, is derived in the appendix.

4. Quadrature correlator noise. Since the inputs to the quadrature correlator each contain a sizable noise component before sampling, it is to be expected that the count developed by the quadrature correlator has a statistical variance or noise component associated with it. This is the noise input to the loop at the output of the correlator shown in Fig. 4. For proper operation of the quadrature correlator within the control loop, this noise must be small with respect to the K in Eq. (16).

K is estimated from the Table 1 data by reference to the probability density curves of Fig. 9. These curves of the baseband signal distribution before sampling are assumed to be Gaussian with means E_i corresponding to the square root of S_i in Eq. (1). Since 2.5 million samples are taken each second, K may be considered to be

$$K = 2.5 \cdot 10^6 \langle X_1 \rangle \tag{17}$$

where $\langle X_1 \rangle$ denotes the statistical mean of X_1, an input random variable to the in-phase correlator counter. In terms of the probability that V_1 is equal to V_2, $P(V_1 = V_2)$

$$\begin{aligned} X_1 = \quad & 1 \text{ with } P(V_1 = V_2) \\ & -1 \text{ with } P(V_1 \neq V_2) \end{aligned} \tag{18}$$

Therefore

$$\begin{aligned} \langle X_1 \rangle &= P(V_1 = V_2) - P(V_1 \neq V_2) \\ &= 2P(V_1 = V_2) - 1 \end{aligned} \tag{19}$$

But

$$\begin{aligned} P(V_1 = V_2) &= P(V_1' > 0)\,P(V_2' > 0) \\ &\quad + P(V_1' < 0)\,P(V_2' < 0) \\ &= P(V_1' > 0)\,P(V_2' > 0) \\ &\quad + [1 - P(V_1' > 0)][1 - P(V_2' > 0)] \end{aligned} \tag{20}$$

where V_1' and V_2' are the baseband signals before sampling. The probability that V_i' is greater than zero is found by integrating the probability density curve for V_i' from zero to infinity. In terms of the error function, erf

$$P(V_i' > 0) = \frac{1}{2} + \frac{1}{2}\,\text{erf}\left(\frac{E_i}{\sqrt{2}\,\sigma_i}\right) \tag{21}$$

where σ_i is the root mean square of the corresponding noise power N_i of Eq. (1) and the error function is defined as

$$\text{erf}\,(x) = \frac{2}{\sqrt{\pi}} \int_0^x e^{-t^2}\,dt \tag{22}$$

Using the notations of Eqs. (12) and (13)

$$R_i = \frac{E_i^2 T_B}{N_{oi}}, \qquad \sigma_i^2 = N_i = N_{oi} B \tag{23}$$

Using Eq. (23), Eq. (21) becomes

$$P(V_i' > 0) = \frac{1}{2} + \frac{1}{2}\,\text{erf}\left(\sqrt{\frac{R_i}{2T_B B}}\right) \tag{24}$$

Using Eqs. (20) and (24), Eq. (19) becomes

$$\langle x_1 \rangle = \text{erf}\left(\sqrt{\frac{R_1}{2T_B B}}\right) \text{erf}\left(\sqrt{\frac{R_2}{2T_B B}}\right) \tag{25}$$

which is evaluated using the values in Eq. (14) and tables of the error function (Ref. 2). From Eqs. (17) and (25), K is found to be approximately 53,000 counts.

The quadrature correlator noise N_y has variance σ_y^2 given by

$$\sigma_y^2 = 2.5 \cdot 10^6 \langle X_2^2 \rangle \tag{26}$$

where X_2 is the random variable into the quadrature correlator counter. Assuming input signals which contain only noise and no data or subcarrier frequency

$$X_2 = \begin{cases} 1 \text{ with probability of } 1/4 \\ -1 \text{ with probability of } 1/4 \\ 0 \text{ with probability of } 1/2 \end{cases} \quad (27)$$

Squaring Eq. (27) gives

$$X_2^2 = \begin{cases} 1 \text{ with probability of } 1/4 \\ 1 \text{ with probability of } 1/4 \\ 0 \text{ with probability of } 1/2 \end{cases} \quad (28)$$

and the mean of X_2^2 is

$$\langle X_2^2 \rangle = 1/2 \quad (29)$$

From Eqs. (26) and (29), the standard deviation, σ_y, of the quadrature correlator noise, N_y, is found to be

$$\sigma_y = 1118 \text{ counts} \quad (30)$$

The ratio of σ_y to K is less than 3% which is highly satisfactory for tracking loop operation.

5. Digital attenuator. The digital attenuator is a left-shift shift register whose number of left shifts is controlled by a front panel thumbwheel switch setting. Each left shift provides a gain attenuation of one half. The circuitry is arranged with respect to the D-A converter of Fig. 4 so that the digital attenuator gain, G_a, is

$$G_a = 2^{R-10} \quad (31)$$

where R is the thumbwheel switch reading, settable from 0 to 15.

6. Digital-to-analog converter. The 16 bit D/A converter may be represented by the well-known zero-order hold circuit described in sampled-data control system texts (Ref. 3). Accordingly, its transfer function, H_d, is

$$H_d = G_d \frac{Z - 1}{Zs} \quad (32)$$

where G_d is a gain constant, s is the Laplace complex frequency, Z is e^{sT}, and T is the sampling period which in this system is one second. Since an input of $\pm 2^{15}$ counts produces an output of ± 10 volts, G_d is

$$G_d = \frac{10}{2^{15}} \frac{\text{volts}}{\text{count}} \quad (33)$$

7. Synthesizer. The frequency synthesizer provides a coherent stable waveform whose frequency is set by front panel switch settings, which in this system is 2.5 MHz. Also contained within the synthesizer is a voltage controlled oscillator called a search oscillator whose output frequency may be algebraically added to the front panel dialed frequency. A ± 10-v control voltage range produces a $\pm \Delta f_s$ search oscillator frequency range where Δf_s may be adjusted in decade steps. Thus the gain of the synthesizer, G_s, is

$$G_s = \frac{\Delta f_s}{10} \frac{\text{Hz}}{\text{volt}} \quad (34)$$

In the present system, Δf_s was set to 10 Hz.

B. Control Loop Analysis

To assure effective phase tracking control loop operation and to determine the limits of phase timing error, the control loop was analyzed for the following:

(1) Loop stability using the root locus method.

(2) Output phase error caused by the input signal characteristics.

(3) Loop jitter caused by the quadrature correlator noise.

(4) Output phase error caused by the search oscillator DC offset.

1. Root locus analysis. Feedback control loop stability is readily found from a root locus analysis which plots in the complex plain the roots of the denominator of the closed-loop transfer function, G_{cl}, as a function of an open-loop gain constant G. In the phase tracking control loop

$$G = G_f G_c G_a G_d G_s T^2 \quad (35)$$

$$G_{cl} = \frac{1}{1 + G_{ol}} \quad (36)$$

where G_{ol} is the open-loop transfer function. From Fig. 4, the open-loop transfer function is found to be

$$G_{ol} = \frac{G}{T^2} \frac{1}{s} \frac{(Z-1)^2}{Z^2} \quad (37)$$

When analyzing systems containing both continuous and sampled-data components, it is customary to convert the entire system into a sampled-data equivalent system. This is accomplished by taking the Z-transform (Ref. 3)

of all relevant equations. Thus the Z-transform of Eq. (37) is

$$G_{ol} = \frac{G(Z+1)}{2Z(Z-1)} \tag{38}$$

and Eq. (36) becomes

$$G_{cl} = \frac{Z(Z-1)}{Z^2 - \left(1 - \frac{G}{2}\right)Z + \frac{G}{2}} \tag{39}$$

The root locus plot is shown in Fig. 10. Since the plot is symmetric about the real axis, only the top half is shown. In the Z plain of sampled-data system analysis, gains which move the poles outside the unit circle cause unstable loop operation. From Fig. 10, it is seen that stable loop operation is obtained for any gain less than 2.0.

In actual operation during the Mariner-Mercury encounter, K's of 100,000 counts were observed. Δf_s was set to 10 Hz as previously stated, and R was set to 4. This provided a loop gain of 0.11.

2. Input analysis. The input analysis determines the steady-state loop error resulting from various types of input functions. From Eq. (38) and Fig. 10, it is seen that a single open-loop pole exists at the value of Z equal to one. Sampled-data control system theory indicates that this condition ensures zero steady-state error for a step input. However, a finite steady-state loop error does exist for an input ramp function. This is of concern since the last entry in Table 1 shows that such a ramp is expected.

To find the steady-state loop error resulting from an input ramp function, reference is made to the input analysis block diagram of Fig. 11, which is a rearrangement of Fig. 4. $R(s)$ is the input time offset Laplace function, and $E(s)$ is the time error output Laplace function. Intermediate Laplace functions within the loop are denoted by X and Y. An asterisk after a Laplace function is used to denote the equivalent sampled-data or Z-transformed function of the indicated Laplace function.

From Fig. 11, the loop equations are

$$E(s) = R(s) - Y^* \frac{1}{s^2} \tag{40}$$

$$X = \frac{G}{T^2}\frac{R(s)}{s} - Y^* \frac{G}{T^2}\frac{1}{s^3} \tag{41}$$

$$Y^* = X^* \frac{(Z-1)^2}{Z^2} \tag{42}$$

Taking the Z-transform of Eqs. (40) and (41) results in

$$E^* = R^* - Y^* \frac{TZ}{(Z-1)^2} \tag{43}$$

$$X^* = \frac{G}{T^2}\left(\frac{R(s)}{s}\right)^* - Y^* \frac{G}{2}\frac{Z(Z+1)}{(Z-1)^3} \tag{44}$$

Solving for E^* from Eqs. (42), (43), and (44) gives

$$E^* = R^* - \frac{\frac{G}{TZ}\left(\frac{R(s)}{s}\right)^*}{1 + \frac{G}{2}\frac{Z+1}{Z(Z-1)}} \tag{45}$$

The steady-state output loop error, E_{ss}, is found by using the final value theorem for sampled-data systems.

$$E_{ss} = \lim_{Z \to 1} ((Z-1)E^*) \tag{46}$$

$R(s)$ for a ramp input is

$$R(s) = \frac{R_a}{s^2} \tag{47}$$

where R_a is the ramp rate constant. The Z-transforms for $R(s)$ and $R(s)/s$ become

$$R^* = \frac{R_a TZ}{(Z-1)^2} \tag{48}$$

$$\left(\frac{R(s)}{s}\right)^* = \frac{R_a T^2 Z(Z+1)}{2(Z-1)^3} \tag{49}$$

From Eqs. (45), (46), (48), and (49)

$$E_{ss} = \frac{R_a T}{G} \tag{50}$$

Using R_a from Table 1, T equal to 1 s, and G equal to 0.11 gives

$$E_{ss} = 25\,\text{ns} \tag{51}$$

3. Noise analysis. The diagram of Fig. 4 may be rearranged to form the Laplace diagram for noise analysis shown in Fig. 12. N_y^* is the quadrature correlator noise, and $J(s)$ is the Laplace function of the time error jitter

signal out of the loop. Since N and J are random processes, it is desired to find the root mean square or standard deviation of J, σ_J. Assuming a flat constant power spectral density for N_y^*, sampled-data noise theory gives

$$\frac{\sigma_J^2}{\sigma_y^2} = \frac{1}{\pi}\int_0^\pi |H_J(Z)|^2\, d\theta, \qquad Z = e^{i\theta} \tag{52}$$

where σ_y is obtained from Eq. (30), $H_J(Z)$ is the transfer function of Fig. 12, and i is the square root of minus one. The equations for Fig. 12 are found similarly as was done for Fig. 11, and $H_J(Z)$ is found to be

$$H_J(Z) = \frac{J^*}{N_y^*} = \frac{\dfrac{G_1 T}{Z-1}}{1 + \dfrac{G}{2}\dfrac{Z+1}{Z(Z-1)}} \tag{53}$$

where G_1 from Fig. 12 is $G/G_c T^2$. Using Eqs. (16), (52), and (53)

$$\sigma_J = \frac{\sigma_y}{0.56\,K}\sqrt{\frac{G}{2}\frac{1+\dfrac{G}{2}}{1-\dfrac{G}{2}}} \tag{54}$$

For σ_y equal to 1118 counts, K equal to 100,000 counts, and G equal to 0.11

$$\sigma_J = 5\,\text{ns} \tag{55}$$

Eq. (54) shows that the loop jitter becomes infinite when G is made equal to 2. This agrees with the determination from the root locus analysis of loop instability at values of G greater than 2.

4. Search oscillator dc offset analysis. The phase tracking loop operates with the search oscillator frequency at zero when the loop is locked to a constant time offset input. If the transfer characteristic of the search oscillator is such that zero frequency out occurs for an input voltage of E_o volts rather than the desired value of zero volts, then the loop at locked conditions will act to generate a search oscillator control voltage of E_o volts. This E_o, called the search oscillator DC offset voltage, represents a finite loop error since zero error would result in a zero quadrature correlator count and a subsequent zero voltage out of the D/A converter.

To minimize this search oscillator DC offset error, careful adjustment of the search oscillator trimming components was made. In addition, a precision adjustable DC compensating circuit was incorporated into the equipment in order to null E_o. Requirements for this nulling were determined from the DC offset analysis Laplace diagram of Fig. 13.

In Fig. 13, a third rearrangement of Fig. 4, $D(s)$ is the Laplace function of the search oscillator DC offset voltage.

$$D(s) = \frac{E_o}{s} \tag{56}$$

$L(s)$ is the Laplace function of the loop error due to the search oscillator DC offset voltage. Using analysis techniques similar to the input analysis of Fig. 11, L^* is found to be

$$L^* = \frac{G_s G_f E_o T}{Z-1}\,\frac{1}{Z-1+\dfrac{G}{2}\dfrac{Z+1}{Z}} \tag{57}$$

From the final value theorem of Eq. (46), the steady-state output error, L_{ss}, is

$$L_{ss} = \frac{G_s G_f E_o T}{G} \tag{58}$$

Using the value of 4 mV for E_o, and the remaining constants as previously indicated, L_{ss} is found to be

$$L_{ss} = 15\,\text{ns} \tag{59}$$

Thus to constrain the loop error due to the search oscillator DC offset to be within 15 ns, the DC offset must be nulled to within 4 mV. Pre- and post-calibration procedures for the encounter mission indicated that this nulling accuracy was indeed accomplished. The sum of the three sources of loop output error described by Eqs. (51), (55), and (59) is equal to 45 ns.

Table 2 lists the signal combiner constants described in the above analysis.

IV. Operational Verification

The actual improvement in signal-to-noise ratio realized by the combining equipment can be estimated from a plot of bit error rate of the processed data over the encounter track period. This plot is shown in Fig. 14. The gradual increase of bit error rate at the beginning and end of the track is due to the lower antenna elevations and hence higher noise inputs at those times.

Toward the end of the track during the time indicated in Fig. 14, the combining equipment was switched out, and only the signal from DSS 14 was processed. During this time, the bit error rate increased from 0.037 to 0.052. This is equivalent to a loss of 0.7 dB in signal-to-noise ratio. Thus the actual improvement due to antenna arraying was within 0.1 dB of the calculated prediction.

V. Conclusion

Analysis of the equipment used to combine the baseband signals from three antennas during the Mariner-Mercury encounter on Sept. 21, 1974 shows that signals arriving at the antennas with a time disparity of over 50 μs were aligned in time to an accuracy better than 50 ns. Moreover, the signals were combined in such a manner as to increase the signal-to-noise ratio of the signal at one antenna by the sum of the signal-to-noise ratios of the signals at the other two antennas. Also shown is that satisfactory equipment operation is relatively insensitive to the key equipment parameters of signal mixing ratios and tracking loop gain.

A plot of the bit error rate during the encounter track shows that the actual combiner improvement in signal-to-noise ratio was 0.7 dB, a value within 0.1 dB of predicted theoretical maximum.

References

1. Wilck, H., "A Signal Combiner for Antenna Arraying," in *The Deep Space Network Progress Report 42-25*, pp. 111–117, Jet Propulsion Laboratory, Pasadena, California, February 15, 1975.
2. Abramowitz, M., and Stegun, A., *Handbook of Mathematical Functions*, National Bureau of Standards Applied Mathematics Series 55, U.S. Government Printing Office, Washington, D.C., June 1964.
3. Kuo, B. C., *Analysis and Synthesis of Sampled-Data Control Systems*, Prentice-Hall, Inc., Englewood Cliffs, N.J., 1963.

Table 1. Design parameters

Symbol	Description	Value
R_1	ST_B/N_0 at DSS 14	1.6 dB
R_2	ST_B/N_0 at DSS 13	−8.4 dB
R_3	ST_B/N_0 at DSS 12	−8.4 dB
	Subcarrier frequency	177.1 kHz
$1/T_B$	Data rate	117.6 kbits/s
	DSS 13 to DSS 14 time delay	28–92 μs
	DSS 12 to DSS 14 time delay	13–67 μs
	DSS 14 microwave round trip delay	110 μs
R_a	Maximum rate of change in time delay of the signals from DSS 12 and 13 with respect to the signal from DSS 14.	10 μs/h

Table 2. Signal combiner constants

Symbol	Description	Value
A_r	Maximum predicted signal-to-noise ratio improvement using arraying	0.8 dB
a_1,a_2	Summing amplifier constants for the baseband signals from DSS 13 and DSS 12	0.3
B	Low-pass filter noise bandwidth	1.57 MHz
G_f	FIFO gain constant	0.4 μs/Hz/s
G_c	Quadrature correlator gain constant	0.56 K counts/μs/s
K	Observed in-phase correlator count	100,000 counts
σ_y	RMS quadrature correlator noise	1118 counts
G_a	Digital attenuator gain constant	2^{R-10}
R	Digital attenuator thumbwheel switch setting	4
G_d	16 bit D/A gain constant	$10/2^{15}$ V/count
G_s	Synthesizer gain constant	$\Delta f_s/10$ Hz/V
Δf_s	Search oscillator decade setting	10 Hz
T	Control loop sampled-data period	1 s
G	Open-loop gain constant	0.11
E_{ss}	Loop output error due to ramp input	25 ns
σ_J	RMS loop jitter	5 ns
E_o	Search oscillator DC offset after nulling	4 mV
L_{ss}	Loop output error due to E_o	15 ns

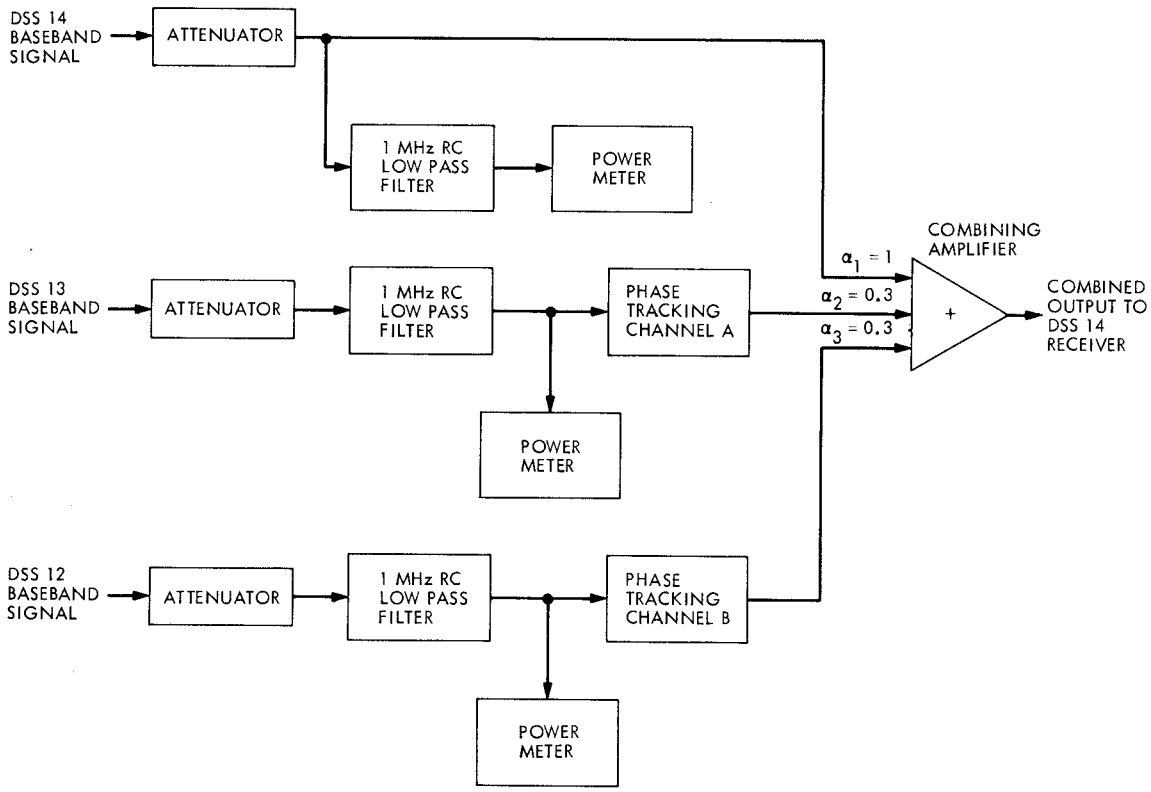

Fig. 1. Signal combiner block diagram

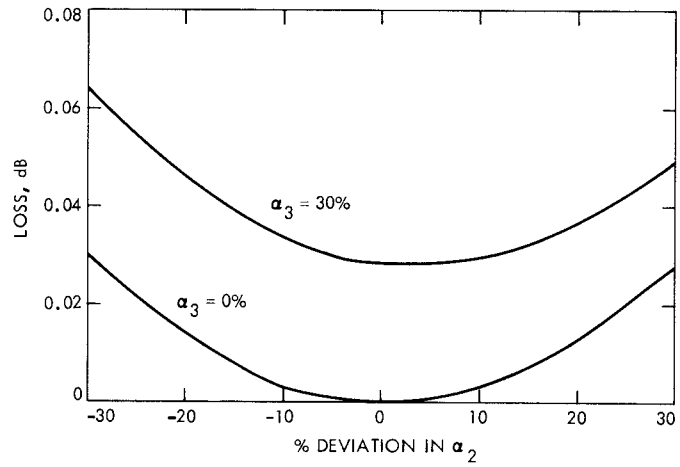

Fig. 2. dB loss for nonoptimum α

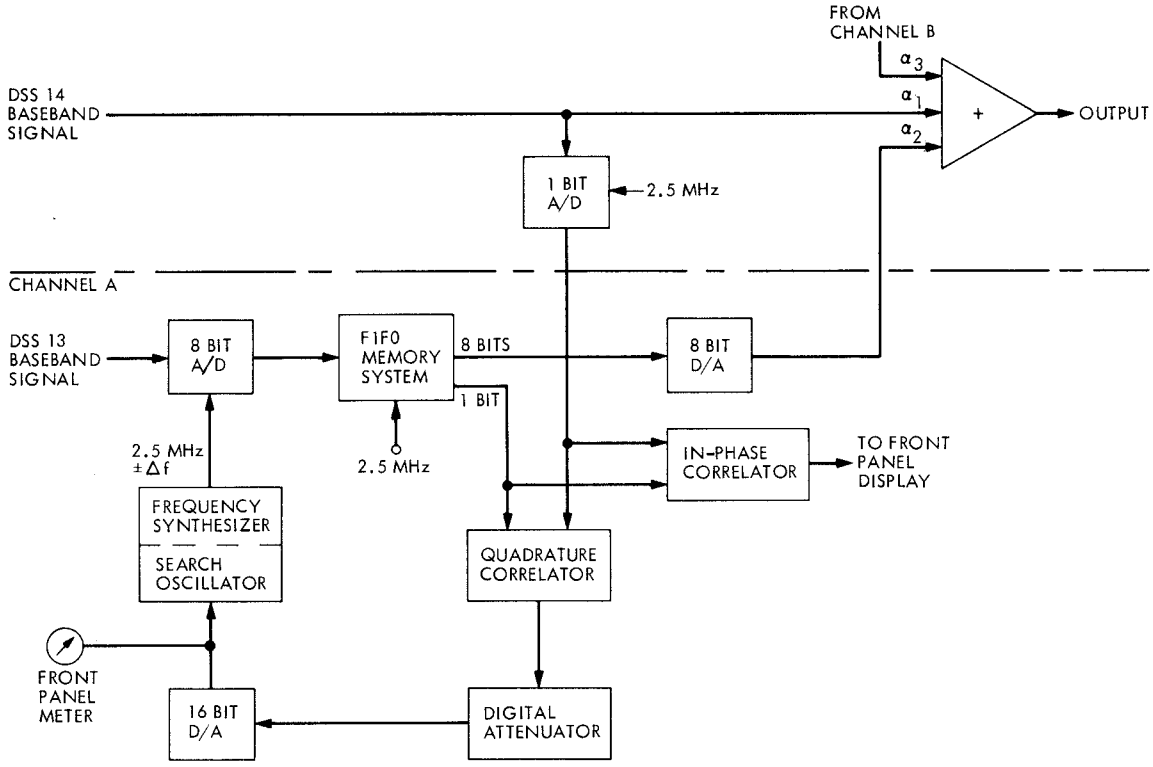

Fig. 3. Phase tracking channel

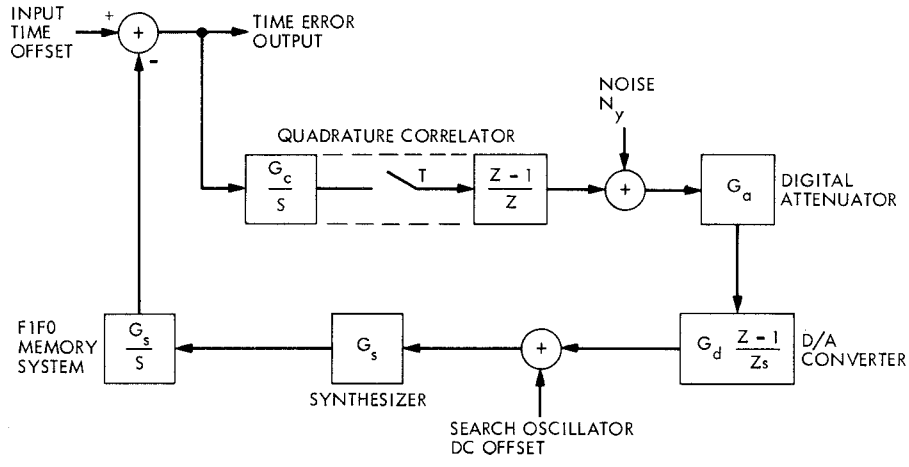

Fig. 4. Laplace block diagram

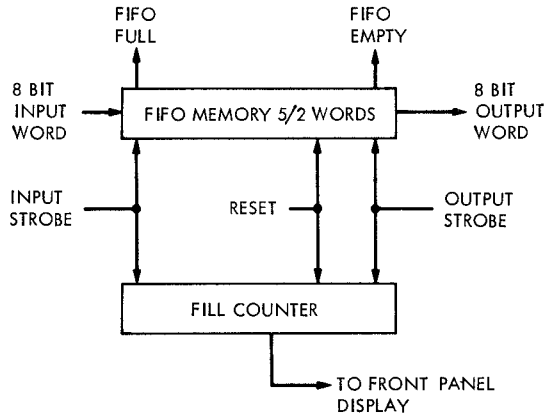

Fig. 5. First-in first-out memory system

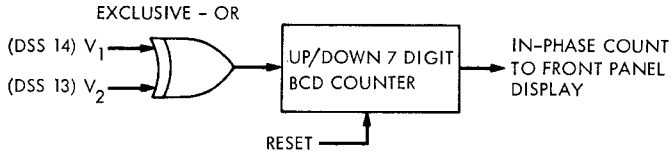

Fig. 6. In-phase correlator

(a) SUBCARRIER ONLY

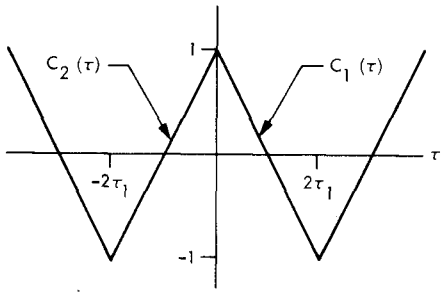

$$C_1(\tau) = 1 - \frac{1}{\tau_1}\tau$$

$$C_2(\tau) = 1 + \frac{1}{\tau_1}\tau$$

(b) PN DATA ONLY

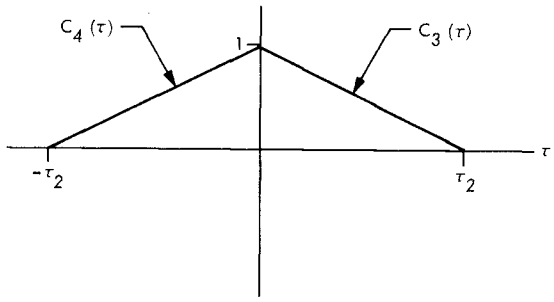

$$C_3(\tau) = 1 - \frac{1}{\tau_2}\tau$$

$$C_4(\tau) = 1 + \frac{1}{\tau_2}\tau$$

(c) SUBCARRIER WITH PN DATA

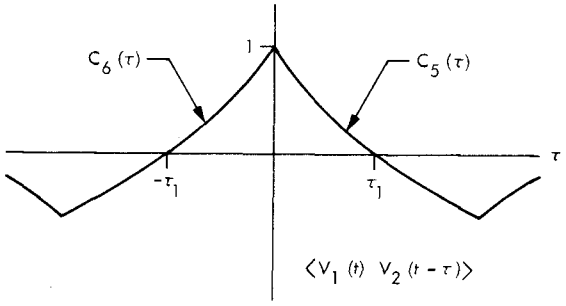

$$C_5(\tau) = C_1(\tau)\,C_3(\tau) = 1 - \left(\frac{1}{\tau_1} + \frac{1}{\tau_2}\right)\tau + \frac{1}{\tau_1\,\tau_2}\,\tau^2$$

$$C_6(\tau) = C_2(\tau)\,C_3(\tau) = 1 + \left(\frac{1}{\tau_1} + \frac{1}{\tau_2}\right)\tau + \frac{1}{\tau_1\,\tau_2}\,\tau^2$$

(d) V_2 DELAYED

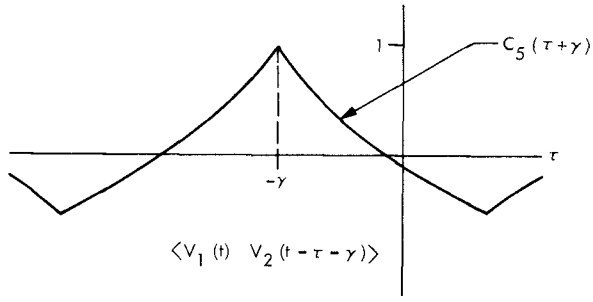

$$C_5(\tau+\gamma) = 1 - \left(\frac{1}{\tau_1}+\frac{1}{\tau_2}\right)\gamma + \frac{\gamma^2}{\tau_1\,\tau_2} - \left(\frac{1}{\tau_1}+\frac{1}{\tau_2} - \frac{2\gamma}{\tau_1\,\tau_2}\right)\tau + \frac{\tau^2}{\tau_1\,\tau_2}$$

(e) V_1 DELAYED

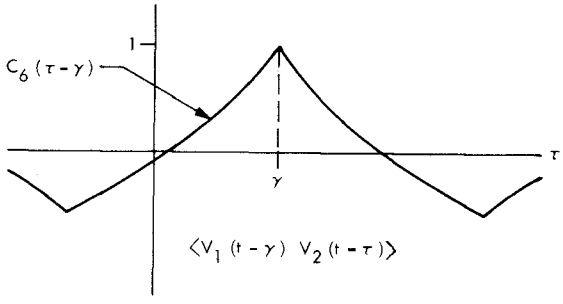

$$C_6(\tau-\gamma) = 1 - \left(\frac{1}{\tau_1}+\frac{1}{\tau_2}\right)\gamma + \frac{\gamma^2}{\tau_1\,\tau_2} + \left(\frac{1}{\tau_1}+\frac{1}{\tau_2} - \frac{2\gamma}{\tau_1\,\tau_2}\right)\tau + \frac{\tau^2}{\tau_1\,\tau_2}$$

(f) QUADRATURE CORRELATOR CURVE

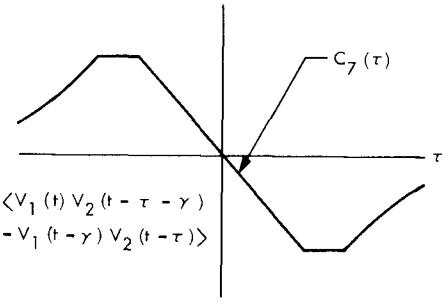

$$C_7(\tau) = \frac{1}{2}\left(C_5(\tau+\gamma) - C_6(\tau-\gamma)\right) = -\left(\frac{1}{\tau_1}+\frac{1}{\tau_2} - \frac{2\gamma}{\tau_1\,\tau_2}\right)\tau$$

Fig. 7. Correlation curves

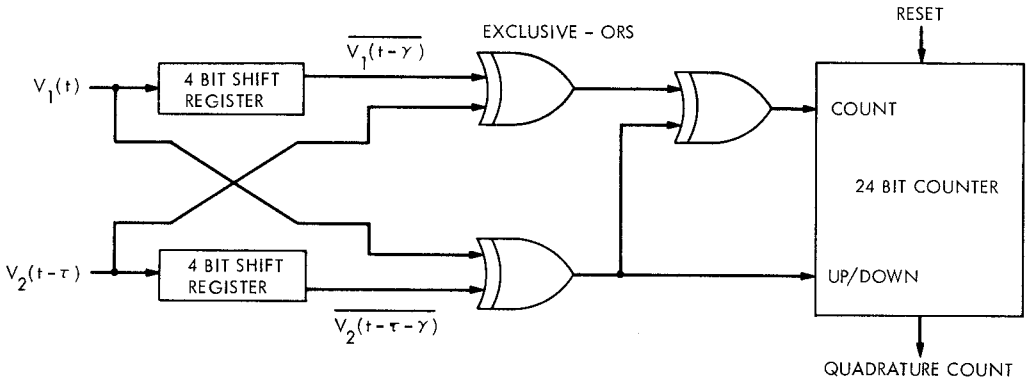

Fig. 8. Quadrature correlator

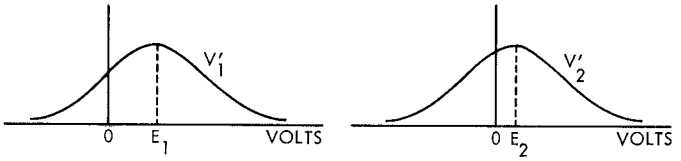

Fig. 9. Probability density curves

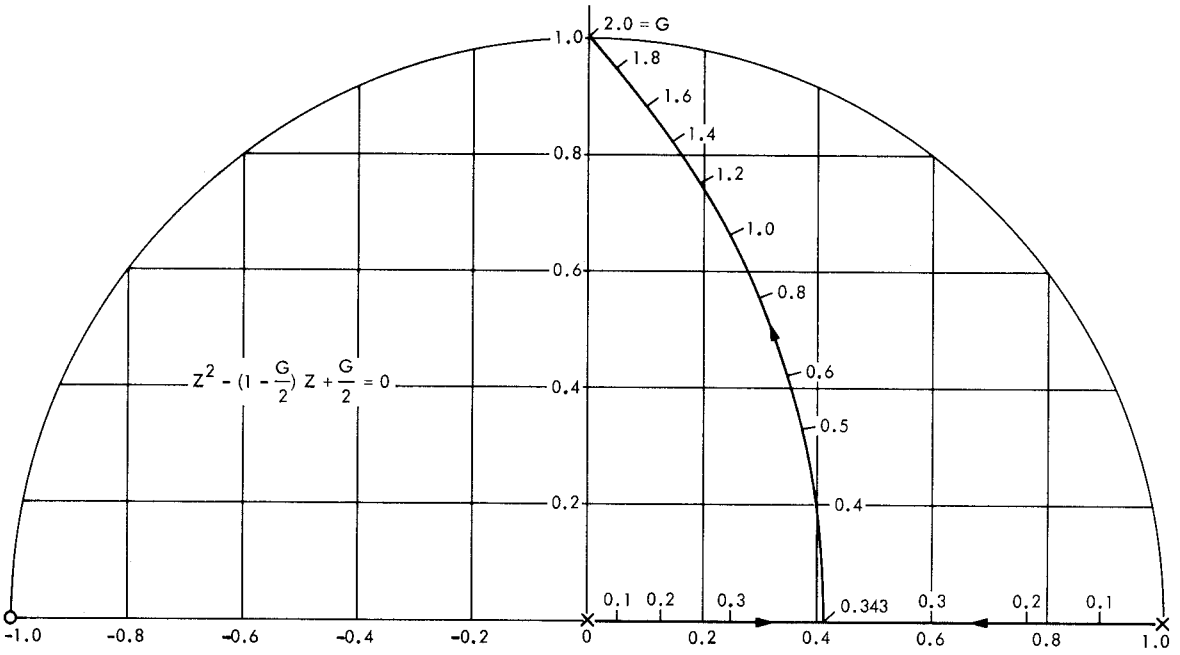

Fig. 10. Phase tracking loop root locus

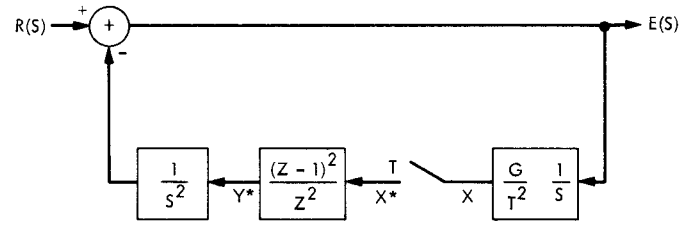

Fig. 11. Input analysis Laplace diagram

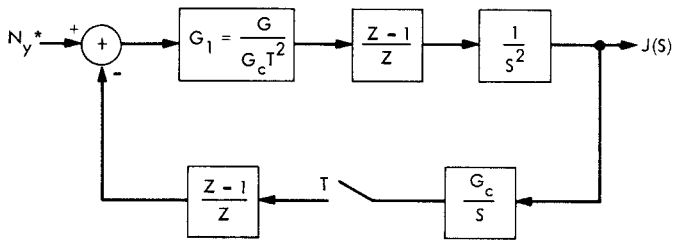

Fig. 12. Noise analysis Laplace diagram

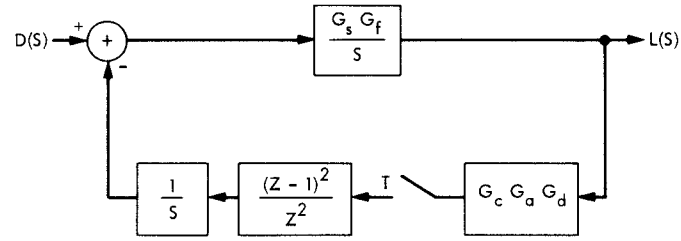

Fig. 13. DC offset analysis Laplace diagram

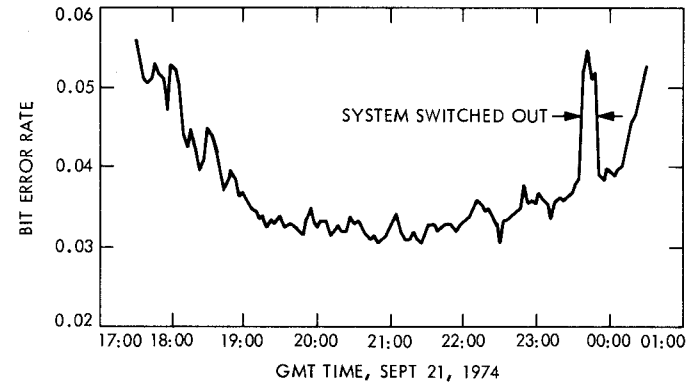

Fig. 14. Bit error rate during encounter

Appendix

Derivation of Integrate-and-Dump Sampled Data Function

A conceptual circuit for the integrate-and-dump function is shown in Fig. A-1. $R(s)$, the Laplace function of the continuous input, is fed to an integrator of gain G. Periodically, at intervals of T seconds, an impulse function is fed to the integrator. This impulse function, properly scaled by the attenuator, sets the integrator output, $C(s)$, exactly to zero. A small amount of pure delay approaching zero in the limit, is required to decouple the zeroing of the output and the formation of the impulse function.

Equations for the loop variables are

$$C(s) = G\frac{R(s)}{s} - X^*\frac{G}{s} \qquad \text{(A-1)}$$

$$X(s) = \frac{1}{G}C(s)\,e^{-\delta sT}, \qquad \delta \to 0 \qquad \text{(A-2)}$$

Since $X(s)$ contains a pure delay term, its Z-transform is

$$X^* = \frac{1}{G}C(Z,m)_{m=1-\delta}, \qquad \delta \to 0 \qquad \text{(A-3)}$$

where $C(Z,m)$ is the modified Z-transform of $C(s)$. Taking the modified Z-transform of Eq. (A-1) and allowing δ to approach zero as a limit gives

$$C(Z,m)_{\substack{m=1-\delta \\ \delta\to 0}} = G\left(\frac{R(s)}{s}\right)^* - X^*\frac{G}{Z-1} \qquad \text{(A-4)}$$

From Eqs. (A-3) and (A-4), X^* is found to be

$$X^* = \frac{Z-1}{Z}\left(\frac{R(s)}{s}\right)^* \qquad \text{(A-5)}$$

and Eq. (A-1) becomes

$$C(s) = G\frac{R(s)}{s} - \frac{G}{s}\frac{Z-1}{Z}\left(\frac{R(s)}{s}\right)^* \qquad \text{(A-6)}$$

$C(s)$ is sampled at the instant before the impulse function sets it to zero. Thus the Z-transform of $C(s)$ is

$$C^* = C(Z,m)_{m=1} = G\frac{Z-1}{Z}\left(\frac{R(s)}{s}\right)^* \qquad \text{(A-7)}$$

A block diagram representing Eq. (A-7) is used for the quadrature correlator in Fig. 4.

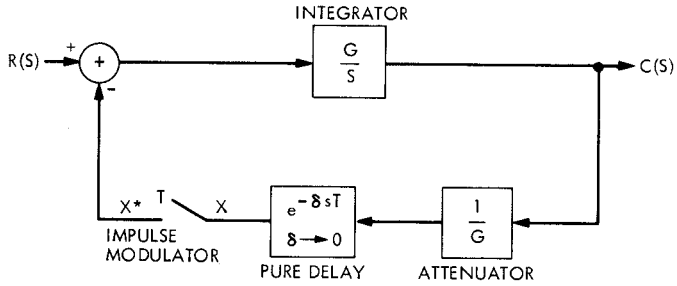

Fig. A-1. Integrate-and-dump Laplace diagram